Characterisation of downwards co-current gas-liquid annular flows

I. Zadrazil[1], C.N. Markides[2], O.K. Matar[3], L. Ó Náraigh[4] and G.F. Hewitt[5]

[1]*Department of Chemical Engineering, Imperial College London, South Kensington Campus, London SW7 2AZ, UK, i.zadrazil06@imperial.ac.uk*

[2]*Department of Chemical Engineering, Imperial College London, South Kensington Campus, London SW7 2AZ, UK, c.markides@imperial.ac.uk*

[3]*Department of Chemical Engineering, Imperial College London, South Kensington Campus, London SW7 2AZ, UK, o.matar@imperial.ac.uk*

[4]*School of Mathematical Sciences, University College Dublin, Belfield, Dublin 4, Ireland, lennon.onaraigh@ucd.ie*

[5]*Department of Chemical Engineering, Imperial College London, South Kensington Campus, London SW7 2AZ, UK, g.hewitt@imperial.ac.uk*

Abstract

The hydrodynamic characteristics of downwards co-current two-phase (gas-liquid) flows inside a vertical tube (ID = 32 mm) have been investigated experimentally. Advanced optical techniques, namely Laser Induced Fluorescence and Particle Tracking Velocimetry, were utilised for the characterisation of these flows over a wide range of gas and liquid superficial velocities ($U_G = 0 – 34$ m·s^{-1} and $U_L = 0.034 – 0.182$ m·s^{-1}), corresponding to Reynolds numbers $Re_G = 0 – 84{,}600$ and $Re_L = 1{,}230 – 6{,}130$. A flow regime map, which contains a previously unreported flow regime, is constructed based on the flow observations. The quantitative analysis of the liquid films allows the generation of film thickness, wave frequency, bubble size, bubble frequency and velocity profile data. It was found that the different observed flow regimes possess a characteristic combination of the investigated quantitative parameters. A model, based on modified mixing-length theory, was used to predict the liquid film velocity profiles and good agreement was found with the experimental results.

1. Introduction

A flow of gas and liquid in a vertical pipe, with the gas phase occupying the central core and the liquid phase flowing in an annulus between the pipe wall and the gas is referred to as ‘annular’ flow. In the special case of downwards annular flow, a flow of liquid on the inner surface of the pipe wall can be formed even at zero gas velocities (the so-called ‘falling film’ case). Annular gas-liquid flows can be found in many important industrial process units, such as condensers, distillation towers, chemical reactors and evaporators.

Downwards co-current annular flows are usually described in terms of flow regimes, which are based on geometrical or topological features of the gas-liquid interface. Webb and Hewitt (1975) identified four different flow regimes with two main classes of interfacial waves: (i) ‘ripple’ waves, and (ii) ‘disturbance’ waves. The former were described as short-lived waves, associated with small spatial amplitudes that quickly decayed, whereas the latter had amplitudes many times (typically a factor of ~ 5) the mean film thickness and high propagation speeds. The four distinctive flow regimes were: (i) the ‘ripple’ regime, where the interface is occupied by a pattern of ripples, (ii) the ‘regular’ wave regime in which disturbance waves traverse the film substrate that is covered with ripples, (iii) the ‘dual-wave’

regime, where two different disturbance wave types coexist, and (iv) the 'thick ripple' regime in which the wave activity decreases with increasing liquid superficial velocity.

Webb and Hewitt (1975) reported further that a critical gas flow-rate exists below which the wave frequency is independent of the gas flow-rate, and hence also the gas superficial velocity (defined as the volumetric flow-rate of the gas divided by the cross-sectional area of the pipe) and the gas Reynolds number. An increase in the gas superficial velocity, above this critical value, then leads to an increase in the wave frequency. Increasing the liquid superficial velocity (liquid volumetric flow-rate divided by the pipe cross-sectional area) was also found to increase the wave frequency. Similar observations concerning the effect of the liquid superficial velocity on the wave frequency were reported by Karimi *et al*. (2000).

Beyond interfacial wave characteristics, Azzopardi (1983) investigated the entrainment of the liquid phase into the gas core, which is another process of prime importance in these flows, both from a fundamental and practical perspective. The author proposed two mechanisms for the liquid entrainment process. During a 'bag' break-up event, that tends to occur at low gas and liquid flow-rates, a part of a disturbance wave is undercut and an 'open-ended' bubble is formed. Build-up of the gas pressure within the bubble results in the expansion of the bubble, which consequently bursts. In the second 'ligament' break-up mechanism, associated with higher gas and liquid velocities, the crests of roll waves are elongated and thin ligaments are torn from the film. One of the objectives of the present paper is to attempt to observe the mechanisms of entrainment in downwards annular flows, and further, to distinguish between these mechanisms and when they are likely to occur.

The importance of annular flow has led to a number of experimental studies (e.g. Azzopardi, 1997; Barnea *et al*., 1982; Koskie *et al*., 1989) that focused mainly on the global (or integral) flow characterisation (i.e. pressure gradients) or used intrusive or point characterisation methods. Downwards annular flows comprise highly localised, small-amplitude and high-speed flow disturbances, and so the characterisation of these flows presents a major challenge from the point of view of experimental design for the provision of detailed and accurate data. Previous measurements (e.g. of film thickness) were performed by using intrusive techniques such as hold-up measurements, hot wire probes or fibre-optics. Non-intrusive measurement techniques, such as conductance probes or acoustic methods, have also been used, but these can only provide temporal measurements at one point (Clark, 2002), and are associated with series of complications, such as an increasingly insensitive signal response at large amplitudes in the case of the conductance probes.

Recently, non-intrusive visualisation techniques, such as Laser Induce Fluorescence (LIF), Particle Image Velocimetry (PIV) and Particle Tracking Velocimetry (PTV) have been used to characterise multiphase flows (Morgan *et al*., 2012). These techniques can allow both the detailed qualitative investigation for these flows, and the reliable and simultaneous evaluation of quantitative flow parameters, such as film thickness, bubble size, and velocity profiles. The present study applies a combination of detailed, spatiotemporally resolved, non-intrusive optical techniques, specifically two-dimensional (2-D) planar LIF (PLIF) and PIV/PTV, to the measurement of downwards co-current gas-liquid annular flows. The measurements using these methods provide qualitative and quantitative data based on which the downwards annular flows can be accurately characterised and mapped.

2. Experimental Methods

The experiments were carried out in the Downwards Annular Flow Laser Observation Facility (DAFLOF) that was constructed to allow the visualisation of flow phenomena occurring in downwards co-current gas-liquid annular flows. The facility is shown in Figure 1(a). The test

section consists of a 3-m long and $D = 32$ mm nominal bore (inner diameter, ID) fluorinated ethylene propylene (FEP) pipe. The ID was selected to match one of the two sections investigated by Hewitt and Webb (1975), for the purposes of direct comparison.

The test gas and liquid were air and water, respectively. The water was circulated through a closed loop by two centrifugal pumps that could be connected either in series or in parallel. The air was taken from the laboratory compressed air supply at 5 – 6 bar and was filtered prior to use. Both air and water flow-rates were measured by turbine flow-meters fitted with a digital display. The manufacturer-stated accuracy of the flow turbines is ± 0.5%, while their repeatability is ± 0.1% of full scale. The water film was injected at the top of the test section using a specially designed injector featuring bevels. The bevels formed a narrow channel through which the liquid was injected in an axial direction down the inner wall of the test section pipe, and formed azimuthally uniform annular liquid films.

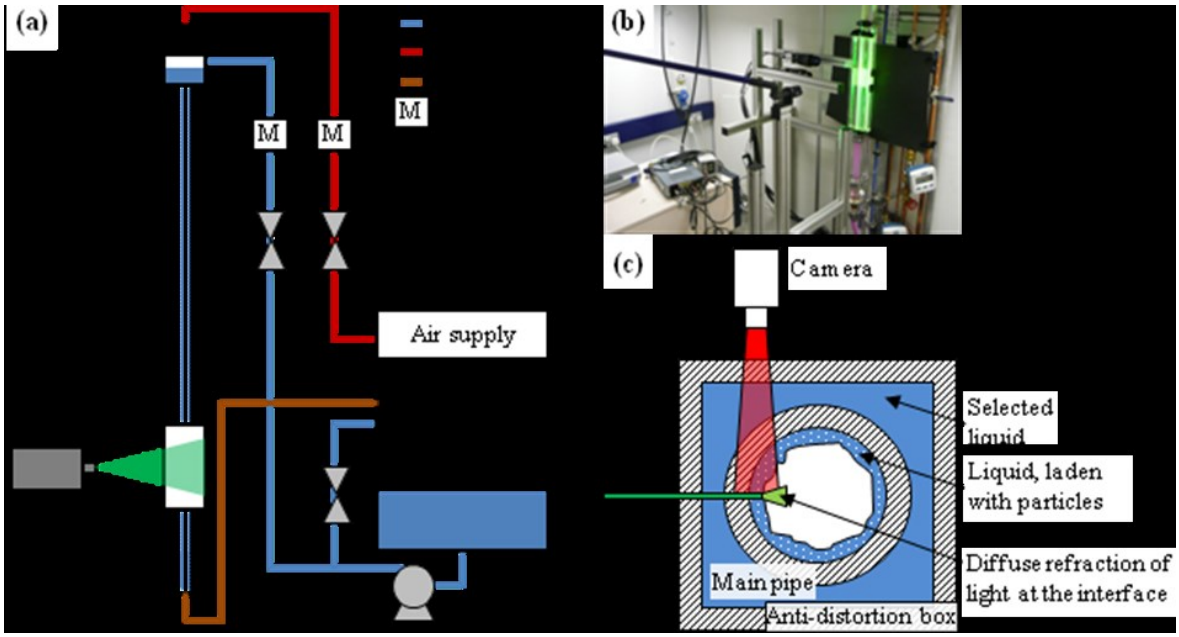

Figure 1: (a) Schematic illustration of DAFLOF, (b) photograph, and (c) simplified schematic illustration of the experimental visualisation setup.

The experimental conditions were chosen in order to operate in the annular flow regime (Kendoush, 1994; Webb and Hewitt, 1975). The investigated superficial gas and liquid velocities, which are both defined over the entire cross-sectional flow area in the pipe $S = \pi D^2/4$, were selected to be in the ranges $U_G = Q_G/S = 0 - 34$ m·s^{-1} and $U_L = Q_L/S = 0.034 - 0.182$ m·s^{-1}, where Q_G and Q_L denote the gas and liquid volumetric flow-rates, respectively. In addition, the corresponding ranges of Reynolds numbers are $Re_G = 0 - 84{,}600$ and $Re_L = 1{,}230 - 6{,}130$. These Reynolds numbers are defined, according to Numrich (1995), based on the pipe diameter D and either the gas or liquid *superficial* velocity U, i.e. as $Re = UD/\nu$, where ν is the gas or liquid kinematic viscosity. The values 1.57×10^{-5} and 9.02×10^{-7} m^2/s have been used for the kinematic viscosities of air and water, respectively. It should be noted that the *liquid* Reynolds number Re_L as defined here is four times larger than film Reynolds number Re_f based on the bulk-mean film velocity $\langle u_f \rangle = Q_L/S_f$ (average volumetric flow-rate Q_L divided by the mean liquid film flow area $S_f = \pi D\langle h \rangle$) and the mean film thickness $\langle h \rangle$, i.e. $Re_f = \langle u_f \rangle \langle h \rangle / \nu_L = (Q_L/\pi D\langle h \rangle)\langle h \rangle/\nu_L = (Q_L/\pi D^2)D/\nu_L = Re_L/4$. For the gas flow, the superficial and bulk velocities are similar, due to the relatively small extent of the overall pipe diameter taken up by the liquid film.

The laser visualisation section was located 2.35 m downstream of the injector, or 74 *D*, in order to allow the flow to develop. Although the mean flow profiles are expected to be fully-developed by this distance from the inlet, it is known from Webb and Hewitt (1975) that these flows continue to evolve *in terms of the mean exhibited wave frequency* for at least 470 *D* (and for at least 160 *D* in terms of the probability distribution of wave thickness amplitude) from the injector. Such lengths were considered prohibitively long for the present investigation, and so it is noted that the frequency data (but not the velocity profile data) are representative of the development region of these flows at a distance of 74 *D* from the inlet.

Considerable effort was made when manufacturing the visualisation section to match of the refractive indices of the three-phases (gas-liquid-solid) in the line of sight of the optical measurement. The purpose of this matching is to minimise any distortion that would arise in the images from the (round) tube test section. The visualisation section was therefore enclosed in a Perspex box with square sides, and the volume between the FEP tube and the internal walls of the Perspex box was filled with de-ionised water (see Figure 1(c)). The refractive indices of FEP and water are 1.34 and 1.33, respectively.

The flow was measured with a PIV/PTV system supplied by LaVision. A photograph of the experimental arrangement is shown in Figure 1(b). The system employs a double-pulsed frequency-doubled Nd:YAG laser, at 532 nm. The flow was seeded with Rhodamine-B dye and Rhodamine-B particles, and was illuminated by a laser sheet from dedicated optics capable of producing sheets of light with a thickness of 0.1 mm at the working distance of ~ 0.5 m, as stated by the manufacturer. The scattered light was recorded by a camera positioned at 90° to the laser light sheet, as illustrated in Figure 1(c). Two mid-speed monochromatic CMOS cameras with 1,280 × 1,024 pixel resolutions and fitted with high-pass filters were used for this purpose, one equipped with a macro-lens. The area visualised for the PLIF and PIV/PTV was 10 × 8 mm, corresponding to a spatial resolution of 7 – 8 μm.

During each measurement a set of 600 image pairs was taken at a frequency of 100 Hz. The raw PLIF images were firstly converted into binarised black and white equivalents by an in-house MATLAB code that used a thresholding approach. The threshold values were chosen as a compromise between small values that were more sensitive in identifying the interface and larger ones that were less sensitive to noise. An example of a raw instantaneous PLIF image and its binarised equivalent are shown in Figure 2(a) and (b).

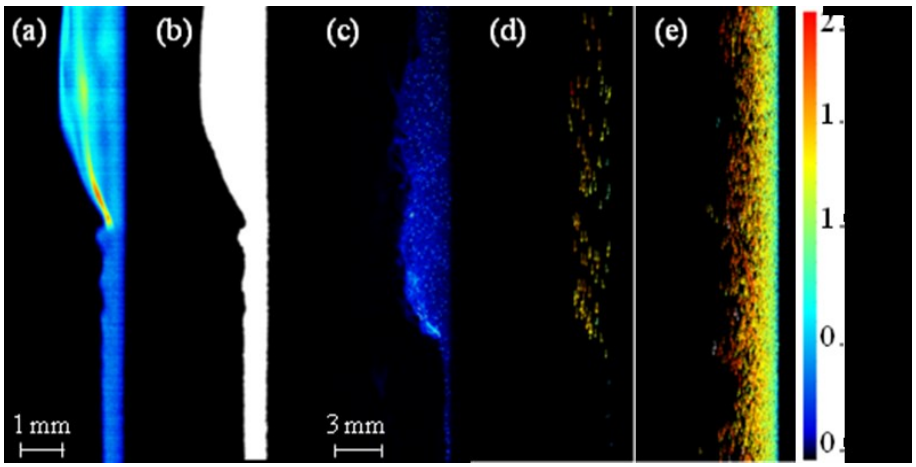

Figure 2: An example of: (a) raw instantaneous PLIF image, (b) binarised equivalent of (a), (c) raw image containing fluorescent particles, (d) instantaneous PTV velocity vector map based on (c), and (e) time-averaged velocity vector map from 600 instantaneous vector maps such as that in (d). The PLIF and PTV images are for a falling film with U_L = 0.034 and 0.134 m·s^{-1}, respectively.

Based on the binarised images, the mean film thickness, wave frequency, bubble size and bubble frequency were calculated. The PIV/PTV calculation was performed in the DaVis environment, supplied by the system manufacturer. Initially the images were pre-processed by subtracting an offset value in order to improve the signal-to-noise ratio (SNR). The calculation of the velocity vectors was done using a multistep cross-correlation approach, whereby reference vectors were calculated using a multi-pass PIV algorithm. The PIV window was first set to 64 × 64 and then to 32 × 32 pixels for the two PIV passes. The velocity information obtained from the PIV was then used as reference for a final PTV calculation in which individual particles were tracked (i.e. each particle yield a velocity vector). Finally, the instantaneous PTV vector maps were time-averaged and the spurious vectors were removed by employing a velocity permissibility range and a median filter. The resulting filtered time-averaged PTV velocity maps were then spatially averaged to yield velocity profiles within the liquid films. Examples of a raw image, an instantaneous and a time-averaged PTV velocity vector map are shown in Figure 2(c) – (e).

3. Results and Discussion

The PLIF and PIV/PTV results have provided new insights into the flow structure of downwards co-current gas-liquid annular flows. Flow regimes as well as phenomenological observations based on the qualitative analysis of the instantaneous PLIF images are presented in Section 3.1. In the succeeding sections the results of the quantitative analysis is presented. Specifically, Section 3.2 presents results on the film mean thickness and large wave frequency. Section 3.3 presents the results for bubble size and bubble frequency. Finally, Section 3.4 shows film velocity profiles obtained from the PIV/PTV measurements, and comparisons to modelling predictions from a modified mixing-length theory approach.

3.1 Flow regimes maps and phenomenological observations

A flow regime map featuring the different flow regimes in terms of superficial gas and liquid velocities, with characteristic corresponding instantaneous images, is shown in Figure 3. The colour of the instantaneous images refers to the intensity of the scattered light.

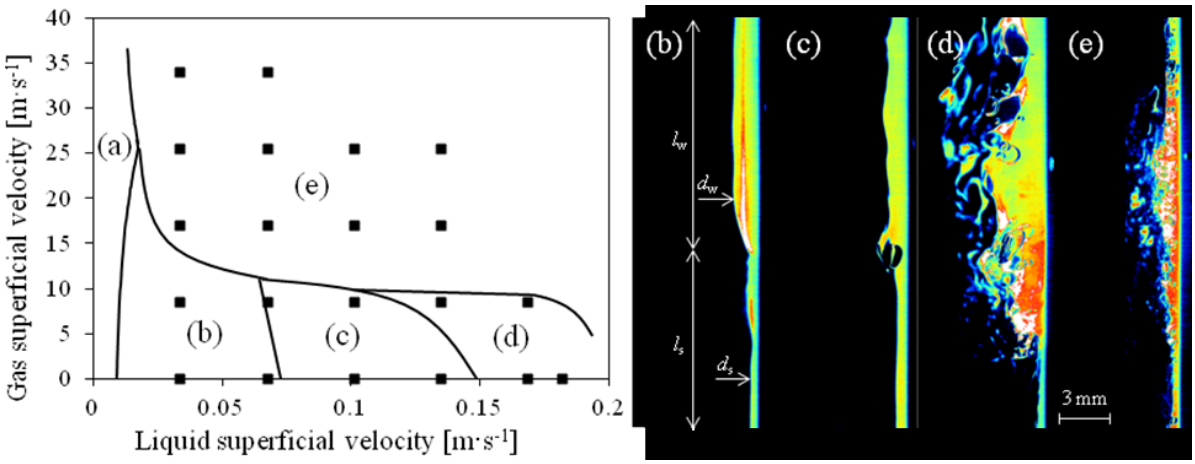

Figure 3: Flow regime map constructed from series of PLIF images and instantaneous images of wave fronts in various conditions. (a) 'Ripple' regime, (b) 'dual-wave' regime ('falling film' with $U_L = 0.034$ m·s^{-1}), (c) 'thick ripple' regime (falling film with $U_L = 0.101$ m·s^{-1}), (d) 'disturbance wave' regime ($U_G = 8.5$ m·s^{-1} and $U_L = 0.135$ m·s^{-1}), and (e) 'regular wave' regime ($U_G = 17.0$ m·s^{-1} and $U_L = 0.034$ m·s^{-1}). The names of the flow regimes (except the newly uncovered disturbance wave regime) are used according to Webb and Hewitt (1975).

Four distinct flow regimes have been observed in the current study. These have been identified based on qualitative observations of the instantaneous PLIF images taking into account the following: (i) substrate thickness h_s, (ii) wave front thickness h_w, (iii) substrate length l_s, (iv) wave length l_w, (v) gas entrainment events into the liquid film, and (vi) liquid entrainment events into the gas core. The definitions of the thickness and length variables are illustrated in Figure 3(b). It should be noted that liquid entrainment events were estimated from the occurrence of bag and ligament break-up types of liquid entrainment into the gas core (Azzopardi, 1983), while gas entrainment events were determined from direct observations of air bubbles penetrating into the water films (e.g. see Figure 3(c)).

The ripple regime was not observed here, due to flow-rate control limitations, and so the flow regime boundary for the ripple regime drawn in Figure 3(a) is taken from Webb and Hewitt (1975). The dual-wave regime, in which no mixing between the two phases was observed, was characterised by large-amplitude waves (with $h_s < h_w$) separated by periods of relative inactivity in which the substrate is longer than the waves ($l_s > l_w$), and was identified when $U_G = 0 – 8.5$ m·s^{-1} and $U_L = 0.034 – 0.067$ m·s^{-1}. The thick ripple regime was observed for falling films over the range $U_L = 0.101 – 0.135$ m·s^{-1}, and for downwards flows when $U_G = 8.5$ m·s^{-1}, $U_L = 0.101$ m·s^{-1}. In this regime large waves occurred sporadically, with the difference between the thickness of the substrate h_s and the wave front thickness h_w, and also between the substrate length l_s and the wave length l_w being minimal, or $h_s \sim h_w$ and $l_s \sim l_w$,. Additionally, the gas was more frequently entrained into the liquid film in the form of bubbles, while liquid entrainment into the gas core via ligament break-up was rarely observed.

Interestingly, a new regime was observed for the falling films at the highest investigated liquid superficial velocities U_L, and also at low superficial gas velocities $U_G = 8.5$ m·s^{-1}. The new regime, termed ‘disturbance wave’ regime, was associated with: (i) $h_s << h_w$, $l_s > l_w$, that is, very large amplitude (disturbance) waves rising clearly above the substrate, with the waves occurring more frequently than in the dual-wave or thick ripple regimes, and (ii) high rates of entrainment of both gas into liquid and liquid into gas. Finally, the regular wave regime was observed for all investigated U_L at $U_G \geq 17$ m·s^{-1}. The flow regime map in Figure 3(a) is in good general agreement with the one reported in the work of Webb and Hewitt (1975).

3.2 Entrainment

Azzopardi (1983) described two different mechanisms of liquid entrainment into the gas phase for vertical upwards flows, namely ligament break-up and bag break-up. Figure 4(a) shows an instantaneous image of ligament break-up, while Figure 4(b) – (e) shows images of bag break-up events at different stages; both are direct observations from our investigated downwards annular flows. Qualitative observations such as these suggest that the mechanism of liquid entrainment into the gas phase might be similar for both downwards and upwards annular flows. Close inspection of many series of instantaneous images (image sequences) indicates that the ligament break-up mechanism is more common than the bag break-up one.

During ligament break-up a number of small liquid drops is formed. On the contrary, bag break-up gives rise to considerable amount of liquid being ejected into the gas phase (see Figure 4(e)). It was also observed that the drops originated from large waves (i.e. disturbance waves), which is in agreement with the findings from the experiments of Azzopardi and Whalley (1980). Following break-up, according to James *et al*. (1980) the re-deposition of drops can be divided into two classes: (i) those that land by diffusion-like process, and (ii) those that arrive by direct impact (i.e. their lateral motion is unaffected). The qualitative observations indicate that the drops created by the ligament and bag break-up mechanisms are responsible for the diffusion-like and direct impact deposition of the drops, respectively.

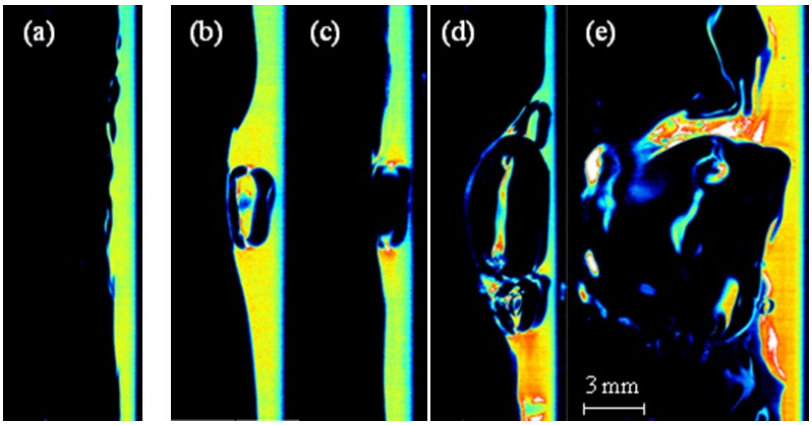

Figure 4: Instantaneous PLIF images of events that lead to entrainment of liquid into the gas phase. (a) 'Ligament' break-up, and (b) – (e) different stages of a 'bag' break-up. The selected images are from falling films at: (a) $U_L = 0.101$ m·s^{-1}, (b) – (c) $U_L = 0.135$ m·s^{-1}, and (d) – (e) $U_L = 0.168$ m·s^{-1}.

3.3 Film thickness and wave frequency

The mean film thickness and wave frequency data are shown in Figure 5(a) and (b), respectively. The error in the measurement of the instantaneous film thickness was ± 0.02 mm. For $U_G \leq 8.5$ m·s^{-1} the mean film thickness increases with increasing liquid superficial velocity U_L with the exception of the flow conditions for which the thick ripple regime was observed (refer to Figure 3). For $U_G \geq 17.0$ m·s^{-1} the mean film thickness $\langle h \rangle$ decreases with increasing liquid superficial velocity U_L or gas superficial velocity U_G. Note that the regular wave regime can be found at these flow conditions.

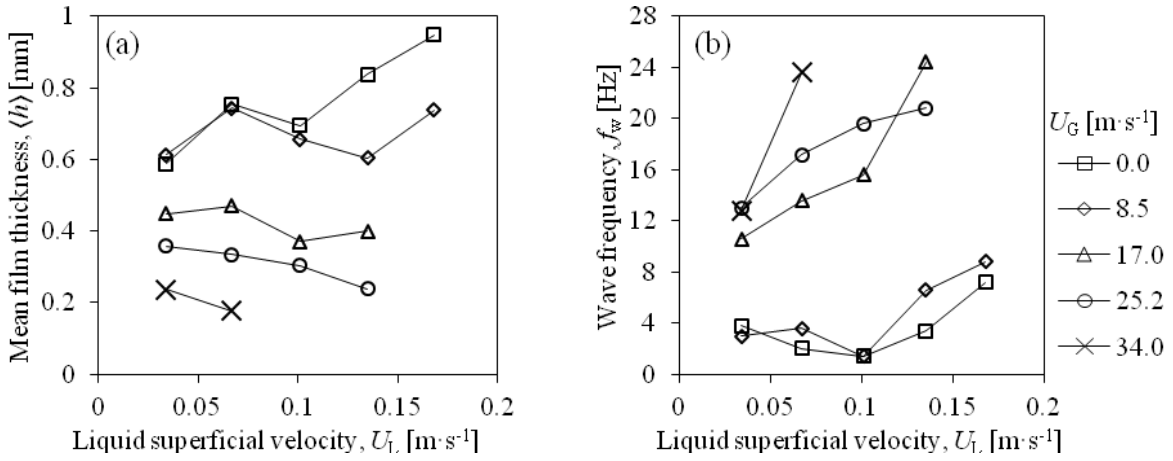

Figure 5: (a) Mean film thickness, and (b) frequency of large waves, for various U_L and U_G.

The wave frequency f_w results are shown in Figure 5(b). It should be noted that a wave is defined is this work as being a disturbance wave if $h_w > 2\langle h \rangle$, where $\langle h \rangle$ is the mean film thickness. In the case of falling films and for the lowest gas velocities $U_G = 8.5$ m·s^{-1} the wave frequency f_w decreases slightly with increasing U_L up to $U_L = 0.101$ m·s^{-1}, reaches a minimum and then increases again. It is useful to recall that the thick ripple regime was observed at the same U_L and U_G associated with the minimum wave frequency f_w. The increase in the observed wave frequency f_w at the higher U_L (> 0.101 m·s^{-1}) ties in with the observations of the new flow regime as discussed above (see Figure 3), in which disturbance waves begin to appear. The result in Figure 5(b) indicates that the disturbance waves become increasingly frequent as the liquid velocity U_L is increased, for a given gas velocity U_G.

At higher gas superficial velocities, specifically for $U_G \geq 17.0$ m·s^{-1}, the frequency of the

large waves f_w increases with increasing U_L and U_G. The sudden increase in the large wave frequency f_w at high U_G (= 34.0 m·s^{-1}) can be explained by the corresponding increase in the shearing force of the gas that *sweeps* the liquid off the tube surface. This results in a thin substrate and relatively thick waves with high gas entrainment, which was indeed confirmed by inspection of the sequences of instantaneous PLIF images.

3.3 Bubble size and bubble frequency

The mean bubble diameter and bubble frequency are shown in Figure 6. The bubble diameters were estimated from direct measurements, which actually represent slices through the bubbles at the position of the laser sheet as these appear in the instantaneous PLIF images. The error in the measurement of the (measured) raw chord lengths was ± 0.05 mm. An assumption was made that an effective mean bubble diameter could be evaluated from the corresponding (measured) mean chord length by multiplying by a factor of π/4. This simple geometric argument assumes that all bubbles are spherical and have the mean bubble diameter. The approximation was checked, in the case of the falling films only, by means of comparison to a more detailed correction procedure in which the mean bubble diameter was evaluated from the knowledge of the full probability distribution of bubbles under the assumption of spherical bubbles occurring uniformly around the circumference of the pipe (Hu *et al*., 2006; Hu *et al*., 2007). The discrepancy between the two approaches was confirmed as being less than 3%.

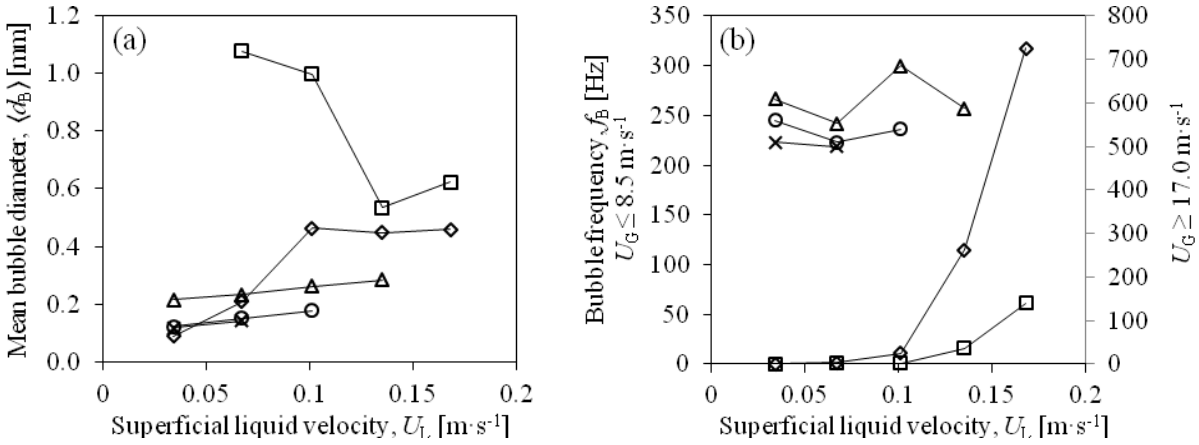

Figure 6: (a) Mean bubble diameter, and (b) bubble frequency for various U_L and U_G. The primary y-axis is for $U_G \leq 8.5$ m·s^{-1} and the secondary y-axis is for $U_G \geq 17$ m·s^{-1}. The legend is identical to that in Figure 5.

The bubble frequency f_B was calculated as the number of bubbles per unit time. For falling films at $U_L \leq 0.101$ m·s^{-1} the level of gas entrainment into the film is negligible, however, the mean size of the bubbles ⟨d_B⟩ was relatively large. The large bubble diameter ⟨d_B⟩ might be explained by the low shear stresses within the liquid film that are insufficient to affect a bubble after it has been entrained. At relatively high U_L or at non-zero U_G the mean bubble diameter ⟨d_B⟩ increases with increasing U_L. The bubble frequency f_B shows an increasing trend for $U_G \leq 8.5$ m·s^{-1} with values of approximately equal to zero for $U_L \leq 0.101$ m·s^{-1}. At high gas superficial velocities (i.e. $U_G \geq 17$ m·s^{-1}) the bubble frequency f_B is independent of liquid superficial velocity and is found to be in the range of 500 – 700 Hz.

3.4 Liquid film velocity profiles

Figure 7(a) shows the measured mean streamwise velocity profiles in the liquid film for the case of falling films with $U_G = 0.0$ m·s^{-1}. In addition, Figure 7(b) – (e) shows mean film streamwise velocity profiles for downwards gas-driven flows with: (b) $U_G = 8.5$ m·s^{-1}, (c) $U_G = 17.0$ m·s^{-1}, and (d) $U_G = 34.0$ m·s^{-1}.

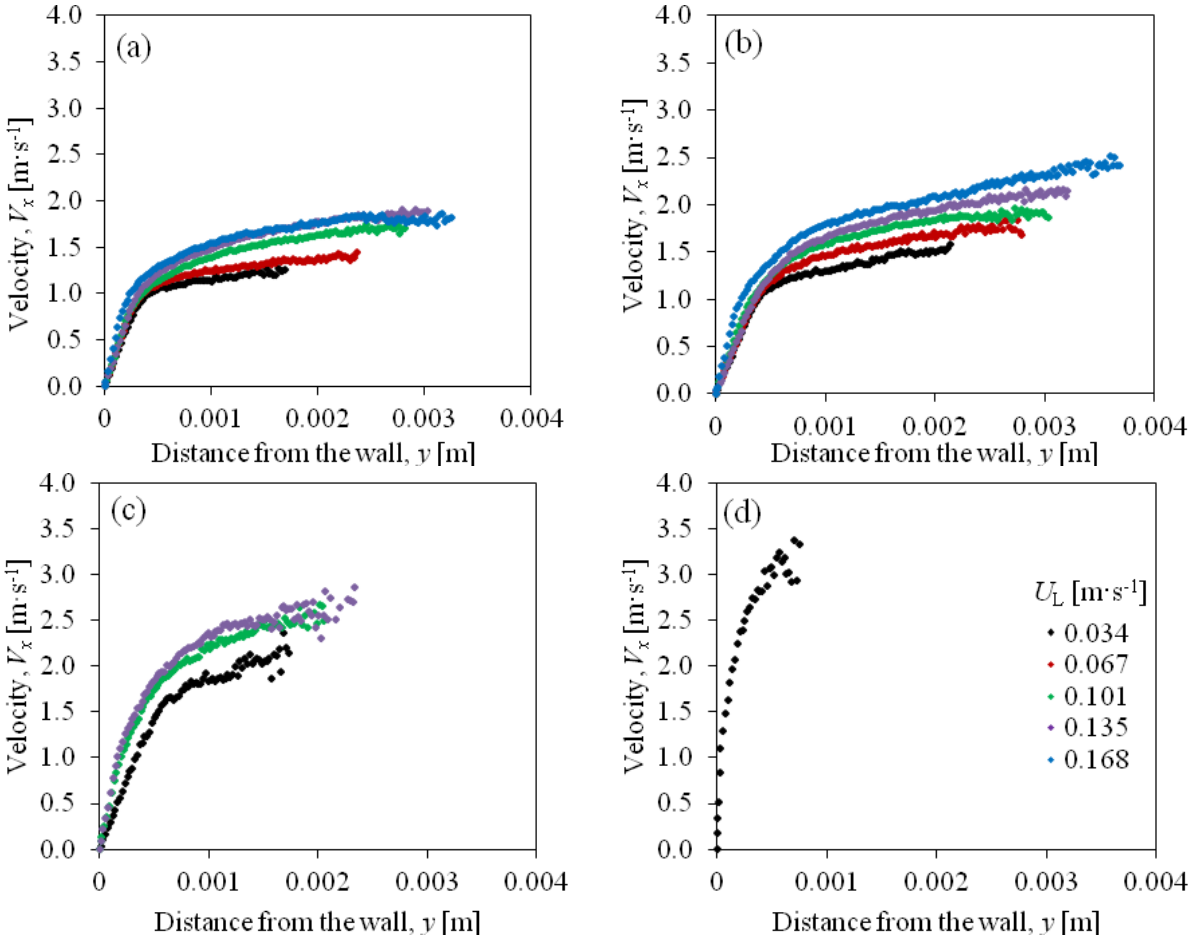

Figure 7: Mean streamwise velocity, V_x, as a function of distance from the wall y for gas superficial velocities: (a) U_G = 0.0 m·s^{-1}, (b) U_G = 8.5 m·s^{-1}, (c) U_G = 17.0 m·s^{-1}, and (d) U_G = 34.0 m·s^{-1}.

Ueda and Tanaka (1975) observed a sharp decrease of velocity in the vicinity of the gas-liquid interface that they attributed to the intermittent nature of the liquid film in the near interface region. No decrease is observable in the present data, though this may be due to the algorithm used that considers the liquid velocity in the intermittent regions as non-existent when the liquid film is not present. From inspection of Figure 7 it can be seen that the film velocity increases with increasing U_L and U_G. The velocity profile for the falling film at the lowest U_L = 0.034 m·s^{-1} follows closely the well-known Nusselt velocity profile (not shown here), as would be expected for laminar flow. At higher U_L and non-zero U_G the velocity profiles diverge and become more turbulent, being steeper near the wall. No discontinuity in the velocity in the vicinity of the mean film thickness (where the boundary between a substrate and a wave can approximately be found) can be observed.

It is possible to obtain an approximation of the mean streamwise velocity profiles for the cases shown in Figure 7 by following an approach employed recently by Ó Náraigh *et al.* (2011) to study the stability of a deformable interface forced by a fully-developed turbulent gas flow in a pressure-driven channel. This approach, which generalises the work of Biberg (2007) to account for near-wall and near-interfacial regions, is adapted for the case considered in the present paper, and illustrated for the specific case of a falling film with and U_G = 0.0 m·s^{-1} and U_L = 0.034 m·s^{-1}.

The Biberg (2007) model assumes the averaged turbulent velocity field to be steady and fully-developed, and employs a modified version of mixing-length theory that introduces an interpolation function for the eddy viscosity (Biberg, 2007; Ó Náraigh *et al.*, 2011). This leads

to similar behaviour to that associated with standard mixing-length theory near the wall and interfacial regions, with a smooth transition from those regions to the bulk. The streamwise mean velocity distribution in the film is then given by,

$$V_x(y) = \int_0^z \frac{c(1-s)}{\frac{1}{Re_f} + \kappa\psi_w(s)G(s)}\,\mathrm{d}s\,, \tag{1}$$

where y is the wall-normal coordinate, $Re_f = \langle u_f\rangle\langle h\rangle/\nu_L$ is the film Reynolds number in which $\langle u_f\rangle$, $\langle h\rangle$, and ν_L denote, respectively, the height-averaged streamwise velocity component, expressed by,

$$\langle u_f\rangle = \frac{1}{\langle h\rangle}\int_0^{\langle h\rangle} V_x(y)\,\mathrm{d}y\,, \tag{2}$$

the mean film thickness, and the kinematic viscosity of the liquid (water); here, we have assumed the film to be sufficiently thin in relation to the pipe diameter so as to be considered planar. The mean film thickness for the $U_L = 0.034$ m·s^{-1} case is approximately equal to 0.0017 m; by digitising and then interpolating the V_x profile for this case, it is possible to use Eq. (2) to obtain $\langle u_f\rangle \approx 1.01$ m.s^{-1}, whence $Re_f \approx 1.87 \times 10^3$.

Returning to Eq. (1), $\kappa = 0.41$ is the von Karman constant, $c = 0.004$, and the functions $G(y)$ and $\psi_w(y)$ are given by,

$$G(y) = y(1-y)(1+[k_f - 1]y), \tag{3}$$

$$\psi_w = 1 - \exp\left(-\frac{y^2}{B}\right), \tag{4}$$

in which $B = \exp(A)/c\,Re_f^2$. Here, $\psi_w(y)$ is a van Driest-type wall-function, which damps out turbulence near the wall, and $G(y)$ is an interpolation function that reproduces the 'law of the wall' near the wall (Ó Náraigh *et al.*, 2011). The value of the interfacial 'roughness' parameter in Eq. (3), k_f (Biberg, 2007), was chosen to be equal to 0.5, while A was set to $A = 7$, corresponding to a laminar sub-layer 6.5 wall-units (Ó Náraigh *et al.*, 2011); these choices were made in order to maximise the agreement between the modelling predictions and the experimentally determined streamwise velocity profile.

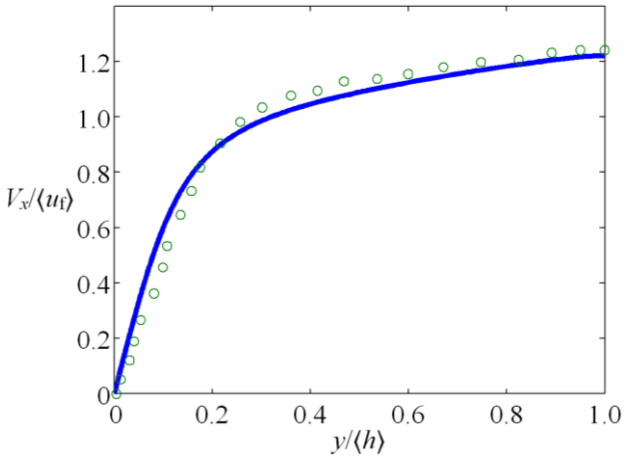

Figure 8: A comparison between the modelling predictions (solid line), based on the work of Biberg (2007) and Ó Náraigh *et al.* (2011), and the experimental data (open circles) for the mean streamwise velocity profile, normalised by its height-averaged value, from Eq. (2). Here, $U_G = 0.0$ m·s^{-1} and $U_L = 0.034$ m·s^{-1}.

The two profiles are shown together in Figure 8. The agreement was found to be relatively insensitive to the value of k_f, within the range $0.5 \leq k_f \leq 1$. It is possible to build on the work of Ó Náraigh *et al*. (2011) in order to generate approximate models for turbulent falling films that capture the transition to wave formation, and nonlinear wave evolution.

4. Conclusions

Non-intrusive laser-based techniques, namely PLIF and PIV/PTV, have been used for the detailed characterisation of downwards co-current gas-liquid annular flows. The analysis of the instantaneous PLIF images revealed the existence of a new disturbance wave regime that occurs at high liquid and low gas velocities. This regime is characterised by a large difference between the wave and substrate thicknesses and by high entrainment rates.

Further analysis of the resulting data yielded information on the film thickness, wave frequency, mean bubble diameter, bubble frequency and of mean velocity profiles, providing a unique insight into the characteristics of downwards annular flows. The following conclusions can be drawn from the analysis of the data:

(1) Two distinct patterns were observed for the measured mean film thicknesses: (i) for gas superficial velocities lower than 8.5 $m \cdot s^{-1}$ the mean film thickness was found to increase with increasing liquid superficial velocity, with the exception of the region where thick ripple regime was observed; (ii) for the flow conditions where the regular wave regime exists, the mean film thickness decreases with increasing gas and liquid superficial velocities.

(2) The wave frequency as a function of liquid superficial velocity showed two different patterns. For gas superficial velocities lower than 8.5 $m \cdot s^{-1}$ the wave frequency followed a parabolic trend with minimum at a liquid superficial velocity of 0.101 $m \cdot s^{-1}$. At higher gas superficial velocities the wave frequency increased with increasing liquid superficial velocity.

(3) The mean bubble diameters observed were of the order of 0.1 – 1 mm. Falling films had the largest mean bubble diameters, except for the lowest liquid superficial velocity where no bubble was observed. Increasing gas superficial velocity at constant liquid superficial velocity resulted in decrease of the mean bubble diameter.

(4) The bubble frequency can be well correlated with the flow regimes. The bubble frequency for dual-wave and thick ripple regimes is lower than 1 and 10 Hz, respectively. In the case of disturbance wave regime, the bubble frequency increases with increasing gas and liquid superficial velocities with maximum of 318 Hz. The highest bubble frequency (500 – 700 Hz) was observed for regular wave regime.

(5) A model, used recently to examine interfacial stability in the presence of turbulence in channel flows, based on the use of modified mixing-length theory, was employed to predict the dependence of the mean streamwise velocity component on the wall-normal direction. The agreement between the modelling predictions and the experimental data was found to be satisfactory.

References

1. B.J. Azzopardi. Mechanisms of entrainment in annular two-phase flow. *UKAEA Report AERE-R 11068*, 1983.
2. B.J. Azzopardi. Drops in annular two-phase flow. *Int. J. Multiph. Flow*, 23: 1-53, 1997.

3. B.J. Azzopardi and P.B. Whalley. Artificial waves in annular two-phase flow. In *Basic Mechanisms in Two-Phase Flow and Heat Transfer (Edited by P.H. Rothe and R.T. Lahey)*, pp. 1-8, ASME, 1980.
4. D. Barnea, O. Shoham and Y. Taitel. Flow pattern transition for downward inclined two phase flow; horizontal to vertical. *Chem. Eng. Sci.*, 37: 735-740, 1982.
5. D. Biberg. A mathematical model for two-phase stratified turbulent duct flow. *Multiphase Sci. Tech.*, 19: 1-48, 2007.
6. W. Clark. Liquid film thickness measurement. *Multiph. Sci. Technol.*, 14: 1-74, 2002.
7. B. Hu, P. Angeli, O.K. Matar, C.J. Lawrence and G.F. Hewitt. Evaluation of drop size distribution from chord length measurements. *AICHE J.*, 52: 931-939, 2006.
8. B. Hu, B., H-m. Yang and G.F. Hewitt. Measurement of bubble size distribution using a flying optical probe technique: Application in the highly turbulent region above a distillation plate. *Chem. Eng. Sci.*, 62: 2652-2662, 2007.
9. P.W. James, G.F. Hewitt and P.B. Whalley. Droplet motion in two-phase flow. *In ANS/ASME/NRC Topical Meeting on Nuclear Reactor Thermalhydraulics*, pp. 1484-1503, 1980.
10. G. Karimi and M. Kawaji. Flooding in vertical counter-current annular flow. *Nuclear Eng. Design*, 200: 95-105, 2000.
11. A.A. Kendoush and S.A.W. Al-Khatab. Experiments on flow characterization in vertical downward two-phase flow. *Exp. Therm. Fluid Sci.*, 9: 34-38, 1994.
12. J.E. Koskie, I. Mudawar and W.G. Tiederman. Parallel – wire probes for measurement of thick liquid films. *Int. J. Multiph. Flow*, 15: 521-530, 1989.
13. R.G. Morgan, C.N. Markides, I. Zadrazil and G.F. Hewitt. Characterisation of horizontal liquid-liquid flows in a circular pipe using simultaneous high-speed laser-induced fluorescence and particle velocimetry. *Int. J. Multiph. Flow*, in peer review.
14. R. Numrich. Heat transfer in turbulent falling films. *Chem. Eng. Technol.*, 18: 171-177, 1995.
15. L. Ó Náraigh, P.D.M. Spelt, O.K. Matar and T.A. Zaki. Interfacial instability in turbulent flow over a liquid film in a channel. *Int. J. Multiphase Flow*, 37: 812-830, 2011.
16. T. Ueda and H. Tanaka. Measurements of velocity, temperature and velocity fluctuation distributions in falling liquid films. *Int. J. Multiph. Flow*, 2: 261-272, 1975.
17. D.R. Webb and G.F. Hewitt. Downwards co-current annular flow. *Int. J. Multiph. Flow*, 2: 35-49, 1975.